Chapter 3

ACTIVE MULTITASKING METASURFACES USING SPACE-TIME MODULATION

The material in this chapter was in part presented in [95].

Active metasurfaces, with their ability to dynamically control optical properties at the subwavelength scale, provide a versatile platform for advanced light manipulation. In the previous chapter, we demonstrated how this characteristic enables the realization of multiple tunable functions using a single metasurface. Example functions included beam steering, engineering of flat-top beams, and multi-beam steering, achieved through an array-level optimization approach [46]. We observed, however, that as the complexity of the target function increases — particularly when simultaneous optimization for multiple tasks is required — relying solely on spatial control of the array's phase and amplitude properties becomes increasingly challenging.

In this chapter, we address this limitation by introducing an additional control variable into the system. Through high-frequency modulation of the applied voltage waveform, we create a *synthetic dimension* [100–102], which enables multiplexing of functionality in the frequency domain. This approach paves the way for metasurfaces capable of performing multiple, dynamically tunable tasks simultaneously by encoding them in distinct frequency channels. We refer to such devices as *active multitasking metasurfaces*.

The chapter begins with a review of the theoretical framework for time modulation and its role in engineering the frequency response from a metasurface. Following a brief review of previous experimental work, we present a proof of concept for electrically tunable space-time metasurfaces, utilizing field-effect tuning in indium tin oxide (ITO) with two interdigitated electrodes [95]. Building on this foundation, we extend the design to include 32 independently addressable electrodes, develop an electronic addressing scheme, and demonstrate active beam switching to tunable angles. Finally, we discuss potential multiplexing strategies for these metasurfaces in various applications and highlight remaining challenges and future directions.

3.1 Space- and time-varying media

Wave propagation at the interface between two isotropic media is governed by Snell's law of reflection and refraction, a fundamental principle of optics that ensures conservation of transverse wave momentum across the interface [103]. Leveraging this principle, bulk optical elements are traditionally designed to introduce gradual, spatially varying changes in the accumulated phase shift of light beams propagating through the medium. In comparison, metasurfaces introduce subwavelength-scale spatial modulations of the refractive index. In passive metasurfaces, this is achieved by carefully designing resonator geometries, and in active metasurfaces by externally modulating the local permittivity. These spatial modulations impart momentum to incoming light, as described by the generalized form of Snell's law [22], detailed in Section 2.1. This approach has enabled the development of various chip-scale optical components, including those for anomalous reflection [23, 104, 105], flat lenses [106–108], and polarization control [109–111].

While spatial structuring of metasurfaces imparts momentum discontinuities in the scattered light, the frequency of light is typically conserved. Although active metasurfaces can change their properties in time, their response is often slow. This characteristic limits their operation to the quasi-static regime (Fig. 1.3), where slow temporal modulations allow switching between different spatial phase gradient configurations while preserving the incident wavelength. In this regime, momentum can be imparted to light, enabling spatial wavefront shaping, but the optical wavelength remains unchanged.

To overcome this limitation, there is increasing interest in time-varying media, which exploit rapid modulations of optical properties (*e.g.*, refractive index) in response to external stimuli. These rapid modulations create a *temporal interface*, analogous to the previously discussed spatial interface, where light momentum is conserved, but its frequency is altered due to energy exchange with the medium [112]. Temporal control of electromagnetic waves has led to the demonstration of exotic optical phenomena such as frequency mixing [113], harmonic beam shaping [93], and the breaking of Lorentz reciprocity [44, 114, 115].

Metasurfaces provide a unique platform for integrating spatial and temporal modulation schemes, enabling the realization of space-time varying media [44, 116–120]. Spatiotemporal modulation of dielectric media has been studied for decades and has produced radio frequency (RF) devices with functionalities such as optical isolation [121], pure frequency mixing [122], and amplification of traveling waves

[123]. Recent advancements in digital coding architectures, in which biasing PIN diodes alters the phase response of the scattered light, have realized a more general spatiotemporal platform for frequency-multiplexed beam steering and shaping at microwave frequencies [93, 124, 125]. At optical frequencies, optical pumping of passive phase gradient metasurfaces consisting of nonlinear optical materials has been demonstrated [112, 126, 127]. However, such systems require the integration of high-power pump pulses, limiting their practicality for many applications.

In this work, we demonstrate electrically tunable metasurfaces that operate at telecommunication wavelengths and are modulated at radio frequencies to achieve spatiotemporal control over the scattered light wavefront and spectrum. Field-effect tunable metasurfaces are ideal candidates for the demonstration of space-time varying media, as they can be modulated with frequencies up to tens of MHz [30]. Our active metasurface employs ITO as an active semiconductor layer that undergoes a change in charge carrier modulation, and therefore dielectric permittivity. As described in Section 2.3, this modulation, combined with a geometrically resonant plasmonic stripe antenna [30, 42], results in a modulation of the reflected light intensity. The strong mode confinement achieved in this design enables localized control over the scattered light properties.

We present two implementations of this design. In the first, stripe antennas are connected to an interdigitated pair of electrodes, and in the second, the metasurface incorporates 32 independently addressable electrodes. These layouts enable uniform reflectance control through collective modulation of all antennas enabling control over the spectrum of light, or the design of two- or multi-level reflectance gratings that generate diffraction of frequency-shifted beams in space, as outlined in the following section.

3.2 Design principle for space-time metasurfaces

Active metasurfaces with individually addressable elements enable dynamic control over light propagation through spatial and temporal modulation schemes. These configurations are illustrated in Fig. 1.3 and include three key cases: (1) quasi-static spatial modulation, (2) purely temporal modulation, and (3) combined space-time modulation. Each case provides unique functionalities for tailoring the momentum and frequency of light.

In the quasi-static configuration (Fig. 3.1a), the metasurface exhibits a spatially varying but time-invariant refractive index profile. The far-field response is described as the summation of electric fields reflected from n metasurface elements, with the response from each element described by

$$E(x, y) = A_n(x, y) \cdot e^{i\varphi_n(x,y)} \cdot e^{i(\mathbf{k}\cdot\mathbf{r}-\omega t)}. \tag{3.1}$$

Here, A_n and φ_n are the amplitude and phase response of each element as function of their spatial position in x and y, $\mathbf{k}$ is the incident wave vector, $\mathbf{r}$ represents the spatial observation point, ω is the frequency of light, and t the time variable. In the ideal case, where a uniform amplitude and 2π phase modulation are achievable through the refractive index modulation, the metasurface can be configured with a spatial phase gradient, as shown in the top row of Fig. 3.1a. This phase gradient imparts tangential momentum to the reflected light, steering it to a desired angle.

For time-modulated metasurfaces (Fig. 3.1b), the refractive index profile varies temporally but remains spatially invariant. In this case, the time-varying reflected electric field scattered from each element can be expressed as

$$E(t) = A(t) \cdot e^{i\varphi(t)} \cdot e^{i(\mathbf{k}\cdot\mathbf{r}-\omega t)}. \tag{3.2}$$

The frequency response of the scattered light is obtained *via* a Fourier transform of $A(t) \cdot e^{i\varphi(t)}$, revealing frequency sidebands offset from the central frequency by integer multiples of the modulation frequency. For ideal metasurfaces configured with a sawtooth phase profile, the primary frequency shift corresponds to the modulation frequency (*e.g.*, 1 MHz in the example shown in Fig. 3.1b), while higher-order harmonics may arise from non-ideal amplitude-phase relations.

Introducing a phase delay α to the driving waveform does not affect harmonic intensities but imparts a phase $l\alpha$ to each harmonic l. This behavior can be used to decouple phase and amplitude and engineer optical wavefronts in space and time. For example, two independent electrodes driven with the same waveform but $\alpha_1 = 0$ and $\alpha_2 = \pi$ produce a binary $0 - \pi$ phase grating that selectively diffracts odd harmonics.

In the general case of space-time modulation (Fig. 3.1c), the resulting scattered field from each element n is described as

$$E(x, y, t) = A_n(x, y, t) \cdot e^{i\varphi_n(x,y,t)} \cdot e^{i(\mathbf{kr}-\omega t+\alpha_n)}. \tag{3.3}$$

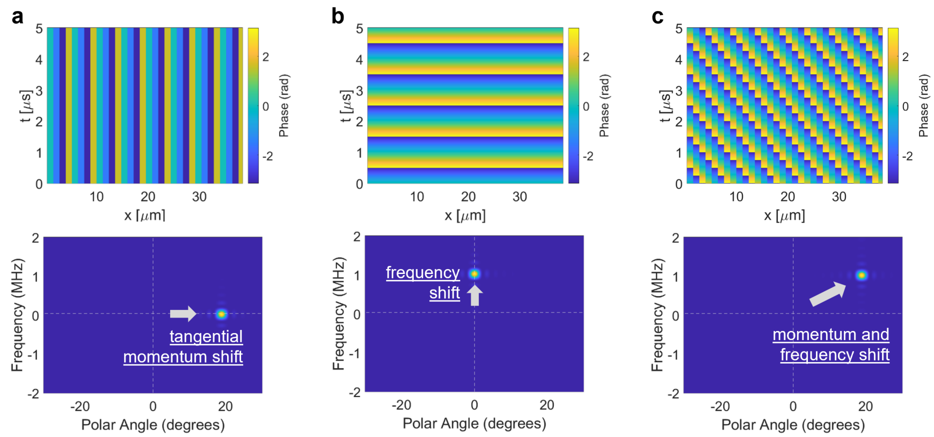

Figure 3.1: **Momentum and frequency-shift with space- and time-modulation.** Top row: Spatial and temporal configuration of phase response from ideal metasurface (2π phase modulation, uniform amplitude) under different modulation schemes. Bottom row: Corresponding frequency spectrum and scattering angle calculations obtained using Fourier transforms in space and time. Three operational regimes are illustrated: (a) quasi-static control with unit cell size of 1.2 μm, (b) time-modulated operation with a 1 MHz sawtooth waveform, and (c) space-time modulation with a phase delay of $\pi/2$ between sawtooth waveforms applied to adjacent unit cells.

For a sawtooth waveform, which produces a single frequency-shifted harmonic with an ideal metasurface, this configuration allows precise steering of the frequency-shifted light. In more complex scenarios involving multiple frequency-shifted beams, tailored waveforms can be engineered for selective steering of target frequencies.

While the examples in Fig. 3.1 assume ideal metasurface arrays with 2π phase modulation and uniform amplitude, practical implementations often exhibit limitations such as reduced phase ranges and covarying amplitude, as discussed in the previous chapter. These limitations lead to the generation of multiple harmonics and variations in the ratios of unmodulated to modulated light. Figure 3.2 demonstrates the changes in the relative conversion efficiency of the 0^{th} and higher order harmonics for a metasurface modulated by a 100 Hz waveform generating a sawtooth phasefront, with varying degrees of phase modulation. The results show that while complete 360° phase modulation suppresses the 0^{th} harmonic and produces a clean $+1^{\text{st}}$ harmonic signal, smaller phase shifts lead to reduced conversion efficiency into the desired harmonic. The specific spectral distribution of a metasurface exhibiting covarying amplitude and phase ultimately depends on the applied time-varying signal and can be analyzed through the Fourier transform of the scattered field.

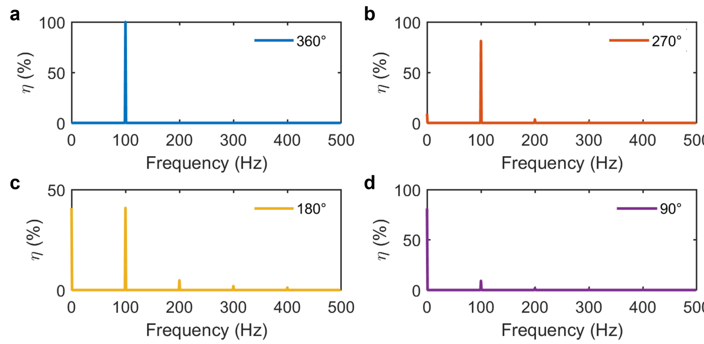

Figure 3.2: **Calculated frequency spectrum of time-modulated metasurface with limited phase modulation.** In all cases, the metasurface is driven with a 100 Hz sawtooth waveform, generating a linearly varying phasefront. The conversion efficiency, η, is presented for phase modulation depths of (a) 360°, (b) 270°, (c) 180°, and (d) 90°. The frequency spectra are obtained through a Fourier transform of the scattered time-modulated fields.

3.3 Time-modulated optical metasurfaces

To experimentally demonstrate time-modulated, and ultimately space-time modulated, metasurfaces, we employ an electrically addressable ITO-based plasmonic metasurface designed to operate in reflection [30]. The design and operational principle align closely with those previously discussed in Section 2.3. We first describe the unit cell design and its quasi-static reflectance properties under applied bias. Subsequently, we introduce the experimental setup for time-modulated measurements and demonstrate how the metasurface response enables tunable frequency shifts under time-modulated operation.

Metasurface design

Figure 3.3a illustrates a unit cell of the active metasurface used in this study. While the carrier modulation mechanism in this ITO-based metasurface mirrors the one described in Fig. 2.9, we adopt a simplified design in this study for ease of fabrication. Each metasurface unit cell comprises a plasmonic stripe antenna over a hafnium oxide/aluminum oxide laminated (HfO_2/Al_2O_3, HAOL) layer and an active ITO layer, forming a metal-oxide-semiconductor (MOS) capacitor heterostructure. This structure is patterned on a gold (Au) back reflector, which serves as the back gate, while the plasmonic gold antenna functions as the top gate. When illuminated with transverse electric (TE) polarized light, a gap plasmon resonance confines light within the ITO and HAOL layers, leading to enhanced optical modulation upon biasing.

In the first part of our study, we design a metasurface with two independent electrodes, each contacting alternating groups of 12 antennas. The entire metasurface measures 120×120 μm^2 (Fig. 2.9b). The two interdigitated electrodes are positioned on the right and left sides of the metasurface area.

Figure 2.9c presents the measured metasurface reflectance under applied bias. The plasmonic resonance, initially at 1475 nm at -4 V, shifts to 1460 nm at 4 V. The operation wavelength throughout this part of the study is 1530 nm. Figure 2.9d shows the voltage-dependent reflectance at this wavelength. The corresponding phase shift at 1530 nm is negligible, as detailed in Appendix B.1. Although the relative modulation is larger on resonance, the shortest wavelength accessible in our experimental setup is 1530 nm, which exhibits a limited relative reflectance modulation ($\sim 8\%$) and near-zero phase shift. Notably, even with these limitations, the device effectively demonstrates space-time diffraction with high directivity, as will be discussed in subsequent sections.

Experimental setup

To study the temporal response of the metasurface, we first modulate all antennas in-phase and measure the reflected frequency spectrum using the experimental setup in Fig. 3.4. The metasurface is illuminated with 1530 nm light which is amplified using an erbium-doped fiber amplifier to enhance the reflected signal strength and enable cleaner measurements. The metasurface is modulated at MHz frequencies using an arbitrary waveform generator (AWG). A fast photodiode connected to a spectrum analyzer captures the reflected light. The output of the spectrum analyzer is fed to a real-time optimization algorithm, which allows the applied waveform to be tailored for a target frequency spectrum. We note that while applied waveforms can be optimized analytically based on the quasi-static response from the metasurface (see Appendix B.2), real-time optimization can account for experimental artifacts, such as changes in the optical response at higher modulation frequencies, ensuring more accurate results, as discussed below.

Because the response times of the photodiode (~10 MHz) and spectrum analyzer (~1 GHz) are many orders of magnitude slower than the oscillation of the incident laser light (~200 THz), only the MHz frequency sidebands imparted on the 1530 nm light are measured. Therefore, the 1530 nm laser light serves as the carrier wave to study the modulation dynamics of the metasurface, while any unmodulated reflected light remains undetected. Since the device primarily operates *via* amplitude

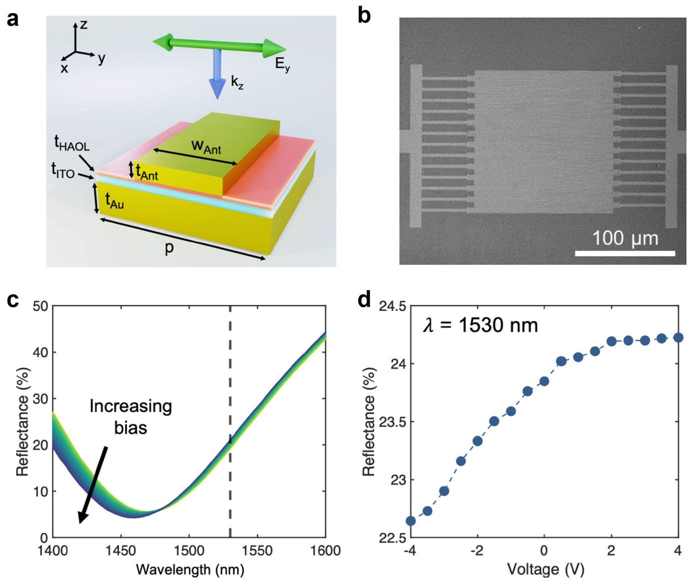

Figure 3.3: **ITO-based plasmonic metasurface and tunable reflectance response.** (a) Schematic of metasurface unit cell. The structure is periodic in the y-axis with a period, p, and extends 120 μm in the x-axis. The metasurface is illuminated from the top with a normally incident plane wave polarized along the y-axis. The dimensions labelled are w_{Ant} = 220 nm, t_{Ant} = 40 nm, t_{HAOL} = 16 nm, t_{ITO} = 17 nm, t_{Au} = 80 nm, p = 400 nm. (b) SEM image of metasurface. The center region creates a 120 x 120 μm^2 active area of nanoantennas which are contacted by the interconnects on either side of the metasurface. Scale bar: 100 μm. (c) Measured reflectance spectra of metasurface under varying applied bias from −4 to 4 V. The dotted line corresponds to the operation wavelength of 1530 nm used throughout this work. (d) Measured reflectance modulation of the metasurface as a function of applied bias at an operation wavelength of 1530 nm.

modulation with minimal phase modulation, a significant portion of the reflected light is unmodulated compared to the frequency-shifted light. However, since only the modulated light is detected using the photodiode and spectrum analyzer, we can study the space-time response with excellent signal-to-noise ratio (SNR) without being limited by the modulation depth. It should also be noted that ITO-based modulators in principle are capable of achieving modulation frequencies up to GHz [128, 129]. Therefore, the MHz-frequency operation in this study is limited by the response time of the photodiode, and not by the metasurface itself.

Control of frequency spectrum

The reflected frequency spectrum of the metasurface can be controlled by applying standard time-varying waveforms to the metasurface (*e.g.*, sine, square, sawtooth).

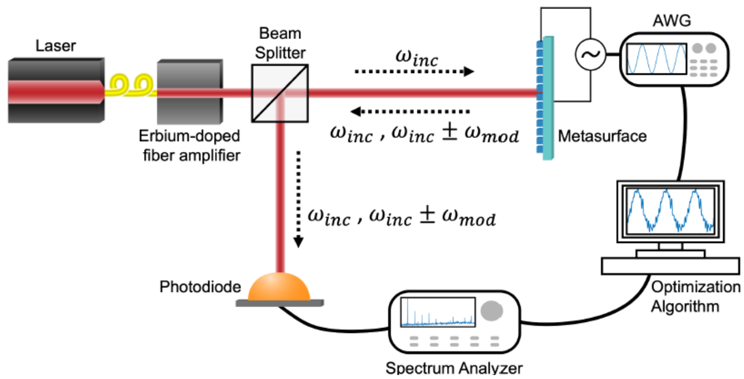

Figure 3.4: **Experimental setup for time-modulated metasurface operation and measurements.** The metasurface is illuminated with a laser at frequency ω_{inc} while being modulated by an arbitrary waveform generator (AWG) that produces a sine wave at frequency ω_{mod}. The reflected light contains both unmodulated components at ω_{inc} and frequency-shifted components at $\omega_{\text{inc}} \pm \omega_{\text{mod}}$. A photodiode connected to a spectrum analyzer detects the reflected signal, which is used as the input for a real-time optimization algorithm which enables optimization to tailor the applied waveform for a target spectrum.

At small applied voltages, the change in reflectance is linear to the applied voltage. As a result, the measured frequency response is directly proportional to the Fourier transform of the applied waveform. Figure 3.5 illustrates frequency spectra obtained using an ITO-based metasurface operating at 1530 nm with characteristics similar to the one depicted in Fig. 3.3. The primary difference is a thicker gate dielectric (t_{HAOL} = 16 nm instead of 8 nm), which necessitated larger voltages to achieve a comparable gate-tunable reflectance response. Measurements in the small-modulation-depth regime were conducted using waveforms with a 6 V peak-to-peak (p-p) amplitude.

Our results demonstrate that the frequency spectrum can be directly tailored by the applied waveform. This is evident from the observed changes when transitioning between sine (Fig. 3.5a, b), square (Fig. 3.5c), and sawtooth (Fig. 3.5d) waveforms. The measured spectra align closely with the frequency components of the applied waveforms, confirming that the metasurface operates primarily through amplitude modulation. Additionally, we note that the metasurface response was measurable up to 10 MHz (Fig. 3.5b), consistent with the the bandwidth limitation of the photodiode used in the experimental setup.

At larger applied voltages, the metasurface enters a regime where its gate-tunable reflectance response becomes non-linear, as shown in Fig. 3.3d. In this regime, the

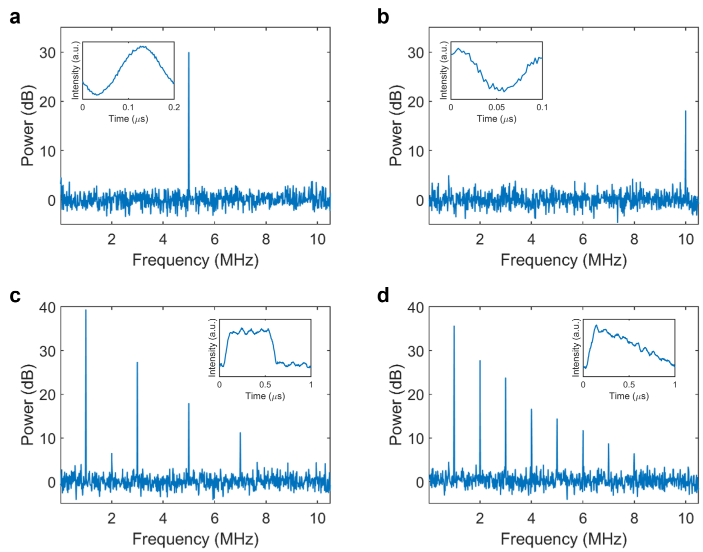

Figure 3.5: **Tunable frequency spectra based on applied waveform.** Frequency spectra of a metasurface illuminated with 1530 nm light and modulated using various waveforms: (a) sine waveform at 5 MHz, (b) sine waveform at 10 MHz, (c) square waveform at 1 MHz, and (d) sawtooth waveform at 1 MHz. The insets display the time-domain reflectance response of the metasurface over a single modulation period.

reflected frequency spectrum deviates from the spectrum of the driving electrical signal when voltages span the full modulation depth. To address this, we implemented an experimental feedback loop that iteratively updates the driving waveform until the desired frequency spectrum is achieved. This approach compensates for non-linearities of the metasurface response as well as other components, such as the metasurface interconnects, the printed circuit board (PCB), waveform generator, photodiode, *etc*. A genetic algorithm was employed to optimize the amplitude and phase of the first 20 terms in a Fourier series, generating the final driving waveform using 1 MHz as the fundamental harmonic.

For an initial demonstration, we optimized the applied waveform to generate only the 1 MHz signal. The top blue curve in Fig. 3.6a shows the initial sinusoidal waveform at 1 MHz, while the red curve represents the final optimized waveform. The corresponding frequency spectra are displayed in Fig. 3.6b. The initial sine wave produces a strong signal at 1 MHz but also generates unwanted power at 2 MHz. In contrast, the optimized waveform maximizes power at 1 MHz while suppressing all other frequencies. We refer the reader to Ref. [95] for details on the optimization algorithm and figure of merit (FOM) selection.

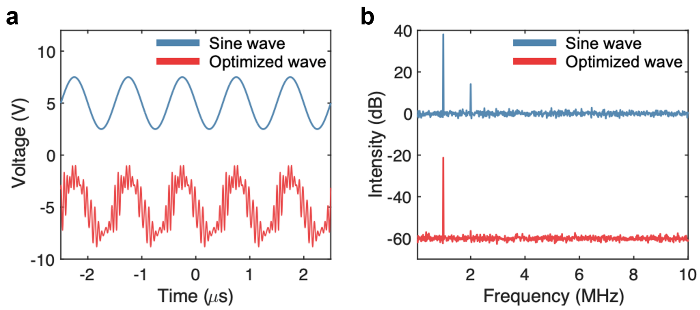

Figure 3.6: **Tailored frequency spectrum using optimized waveform.** (a) Driving voltage waveforms applied to the metasurface shown in Fig. 3.3: a 5 Vp-p sine wave (blue) and the optimized waveform (red). (b) Corresponding reflected frequency spectra for the sine wave (blue) and optimized waveform (red). Both the waveforms and frequency spectra are vertically offset for clarity in visualization.

The optimized waveform includes frequency components up to 20 MHz, exceeding the 3 dB cutoff of the photodiode at 10 MHz, and is therefore partially filtered during the experiment. However, it was found that incorporating these higher frequency components improved suppression of higher-order harmonics. The optimized waveform generates time-domain reflected signals that more closely approximate a sine wave, while the unoptimized sinusoidal input results in a distorted response due to the non-linear reflectance behavior from the metasurface [95]. In Ref. [95], we further illustrate how the FOM can be adapted to obtain tailored waveforms that yield desired harmonics with target relative amplitudes.

3.4 Space-time modulation: Diffraction of frequency-shifted beam

Space-time metasurfaces have the ability to spatially manipulate wavefronts across the generated spectrum, enabling distinct tasks to be encoded for individual harmonics. While detailed discussions on spatio-temporal configurations for controlling specific harmonics are presented in Section 3.6, this section focuses on the experimental demonstration of diffraction for a single frequency-shifted harmonic using the two-electrode metasurface layout introduced in Fig. 3.3b. Figures 3.7a and b illustrate two driving schemes under investigation. In both cases, the metasurface is driven with the optimized waveform from Fig. 3.6.

In the first driving scheme, the two antenna groups are modulated in-phase (Fig. 3.7a). Along with the previously presented frequency spectrum in Fig. 3.6b, we measure the frequency spectrum at both the 0^{th} and $+1^{\text{st}}$ diffraction orders by positioning the photodiode accordingly. In this configuration, nearly all the reflected 1 MHz signal is in the 0^{th} order, with a small signal detected at 1 MHz in the $+1^{st}$ diffraction order. This minor signal is likely due to slight differences in the amplitude/voltage response between the two independent antenna groups.

In the second driving scheme, the two antenna groups are modulated out-of-phase, with the two waveforms phase-delayed by half a waveform period (π), as schematically depicted by the blue and orange colors in Fig. 3.7b. Under this scheme, our measurements reveal that the 1 MHz signal in the $+1^{st}$ diffraction order is approximately 12 times greater than the signal in the 0^{th} order. The small residual signal at the 0^{th} order is attributed to variations in the average reflectance of the entire metasurface in time, caused by the applied waveform as well as the aforementioned discrepancies in the amplitude/voltage response of the antenna groups.

To comprehensively evaluate the space-time performance of the metasurface, we employ the second driving scheme (Fig. 3.7b) and spatially scan the photodiode in Fourier space (Fig. 3.4). This approach allows us to measure the frequency spectrum at incremental positions, generating an intensity map of the reflected light as a function frequency and angle (Fig. 3.7c). The left panel displays the measured data, while the right panel shows spatial cross-sections of the measured intensity for each integer harmonic of the modulation frequency.

Despite the strong absorption in the metasurface and its reliance on amplitude modulation (which does not suppress unmodulated light), we observe that 94% of the modulated light power is in the $\pm 1^{st}$ diffraction orders at 1 MHz. This represents a significant improvement in performance compared to the quasi-static diffraction achievable with amplitude rather than phase modulation [95]. It is important to note that the limited absolute efficiency of the metasurface stems from the specific device design used in this study and does not present a fundamental limitation of the proposed method. In Section 3.7 and the subsequent chapter, we present pathways toward achieving higher efficiency metasurfaces.

3.5 Tunable diffraction of frequency-shifted beams

Until now, we have utilized a metasurface design based on a pair of interdigitated electrodes, which restricts spatial wavefront engineering to active switching of diffracted beams at a design specific angle that is fixed during fabrication. To enhance versatility in the spatial domain, we extended the design to a 32-electrode ITO-based metasurface. While active metasurfaces with an increased number of independently addressable electrodes have been demonstrated previously [42], time-

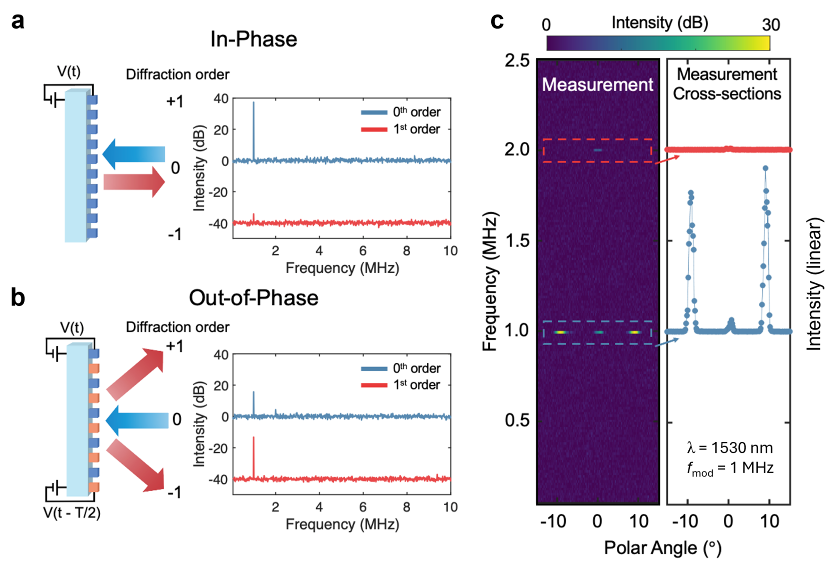

Figure 3.7: **Diffraction of a single harmonic with two-electrode metasurface.** Throughout this figure, the metasurface is modulated using the red optimized voltage waveform shown in Fig. 3.6a. (a) All metasurface antennas are modulated in-phase. Left: Schematic representation of the metasurface response. Right: Measured frequency spectra with the photodiode positioned at the 0^{th} (blue) and $+1^{\text{st}}$ (red) spatial orders. (b) The driving waveform is applied to the metasurface antennas, with adjacent antenna groups modulated out-of-phase by half a period (π). Left: Schematic of metasurface response. Right: Measured frequency spectra with the photodiode positioned at the 0^{th} (blue) and $+1^{\text{st}}$ (red) spatial orders. (c) The metasurface is driven under the out-of-phase condition from (b). Left: Measured intensity of reflected light as a function of frequency and angle, plotted in log scale. Right: Spatial intensity cross-sections from the left panel, plotted in linear scale at 1 MHz (blue) and 2 MHz (red).

modulation introduces the additional challenge of high-frequency electrical addressing of the metasurface, which necessitates sophisticated design of the control PCB.

In this section, we first present the layout of the 32-electrode metasurface and detail the high-frequency circuit board necessary for space-time modulation. We then demonstrate the integration of the metasurface with the PCB, showcasing its ability to achieve quasi-static diffraction and steering of beams to tunable angles. Finally, we analyze the spatio-temporal performance of this metasurface and conclude with a discussion on potential future improvements and measurements that could be applied to this design.

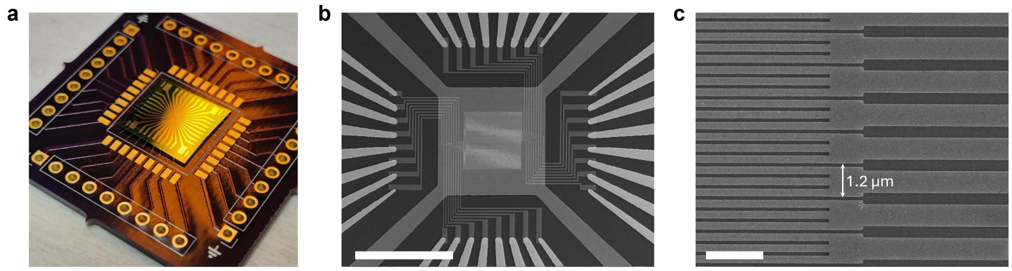

Figure 3.8: **Plasmonic ITO-based metasurface with 32 independently addressable electrodes.** (a) Metasurface chip integrated onto an adapter PCB *via* wire bonding. (b) SEM image of the metasurface showing 4×8 independent interconnects on each side and 4 common ground gates leading to each corner. The stripe antennas are oriented along the horizontal direction. The central $\sim 40 \times 120\ \mu\text{m}^2$ region of the metasurface is connected to 32 independent electrodes, while the top and bottom thirds are shorted. Scale bar: 200 μm. (c) Each electrode controls three stripe antennas, resulting in an effective period of 1.2 μm. Scale bar: 2 μm.

Metasurface layout and fabrication

A unit cell of the 32-electrode metasurface consists of the same stripe antenna design as shown in 3.3, with a period of $p = 400$ nm. Similar designs with a 400 nm period have previously been used to realize multifunctional metasurfaces with 96 independently addressable electrodes [42, 46]. Here, we reduce the number of electrodes to 32 to realize a more compact chip that can be seamlessly integrated into the optical setup. Additionally, reducing the number of electrodes minimizes the risk of shorted interconnects through the formation of pinholes during the wire-bonding process.

Figure 3.8a depicts the 32-electrode chip integrated into an adapter PCB, which is subsequently mounted onto the driving PCB. Each chip measures 1×1 cm^2 and features eight top electrodes and one ground electrode on each side. All ground electrodes are connected to the common back reflecting plane. A close-up of the metasurface with its top and bottom electrodes is shown in the SEM image in Fig. 3.8b. The central metasurface area, measuring $120 \times 120\ \mu\text{m}^2$ contains horizontally oriented stripe antennas. Within this area, the central $\sim 40 \times 120\ \mu\text{m}^2$ region is addressed with 32 independent electrodes, while the top and bottom thirds are shorted to the top- and bottommost electrodes, respectively. In the central tunable region, each electrode controls three stripe antennas, resulting in an effective period of 1.2 μm, as shown in Fig. 3.8c.

The metasurfaces are fabricated on 2-inch Si wafers with a 1 μm thick thermally grown silica (SiO_2) layer for electrical isolation. The wafers are first cleaned using RCA 1 and RCA 2 cleaning procedures. The Au back layer and back contacts are patterned using photolithography with a bilayer photoresist (LOR7B and S1805). Following this, 5 nm titanium (Ti) and 80 nm Au are deposited using electron beam (e-beam) evaporation, and liftoff is performed in Remover PG. Next, the ITO layer is patterned using e-beam lithography with a bilayer polymethyl methacrylate resist (PMMA, 495 PMMA A2 and 950 PMMA A2). A 10 nm ITO is then deposited using RF sputtering with a 90/10 wt% indium oxide/tin oxide (In_2O_3/SnO_2) target at 3 mTorr and 100 W, while flowing 20 sccm argon (Ar) and $7 - 8.5$ sccm of an argon/oxygen (Ar/O_2, 90/10 wt%). The Ar/O_2 flow rate is adjusted to control the ITO carrier concentration, with higher carrier concentrations resulting in redshifted resonances. After liftoff in Remover PG, the HAOL layer is deposited through thermal atomic layer deposition (ALD) at 150 °C using a shadow mask. The deposition consists of two cylcles of 1 nm Al_2O_3/6 nm HfO_2, without breaking vacuum, to achieve a total thickness of 14 nm. The stripe antennas and inner interconnects are then patterned using e-beam lithography with a bilayer PMMA resist (495 PMMA A4 and 950 PMMA A2). A 2 nm germanium (Ge) adhesison layer and 40 nm Au layer are e-beam evaporated, followed by liftoff in Remover PG. Finally, the top contact pads are patterned using photolithography (S1813 photoresist), deposited using e-beam evaporation of 20 nm Ti and 200 nm Au, and lifted off in Remover PG. The completed devices are diced into 1×1 cm^2 chips and wire bonded into PCBs.

We note that the layer thicknesses, ITO carrier concentration, and stripe antenna widths were varied during each fabrication round to achieve strong phase modulation at target wavelengths between $1530 - 1560$ nm. Although some devices successfully achieved this target, the experimental demonstrations of space-time metasurfaces below mostly relied on amplitude modulation.

Design of high-frequency circuit board

A straightforward control board design with 32 individual electrodes, each connected to multiple AWG inputs, can suffer from excessive spatial requirements and significant crosstalk when signals are applied at MHz frequencies. To address these challenges and enhance bandwidth, we developed a compact PCB design that eliminates the need for multiple ribbon cables. Signals from the AWG are delivered to the metasurface using controlled-impedance coaxial lines, which are properly terminated at the board to ensure signal integrity. Additionally, high-bandwidth integrated circuit (IC) amplifiers are used to locally buffer the signals, further reducing crosstalk and ensuring stable signal operation.

The PCB incorporates two AD8113 multiplexers (MUXs), each capable of redirecting up to 16 inputs to 16 outputs. In our implementation, the two MUXs are configured to accept up to 8 inputs from a function generator and dynamically route them to any of the 32 metasurface electrodes. This routing is managed by an Arduino-compatible microcontroller unit (MCU, Teensy 4.1), enabling real-time programmable control. The MCU is powered by a 5 V bench top power supply, and commands are sent using the Arduino IDE.

To extend the functionality of the circuit board, we implemented full 32-channel support with both analog-to-digital converters (ADCs) and digital-to-analog converters (DACs) using the AD7616 (ADC) and LT2688 (DAC) chips. This design enables synchronous voltage control across all 32 channels with arbitrary waveforms at a sampling rate of approximately 40 μs, corresponding to modulation frequencies of up to 25 kHz. By comparison, modulation frequencies for AWG-driven metasurface control are constrained by the AD8113 multiplexers, which have internal buffers limiting their usable bandwidth to the $3 - 10$ MHz range.

Figure 3.9 illustrates the control board, which has a compact size of 3.6×4.6 inches. To maintain this compact footprint, the IC side of the board (Fig. 3.9a) is equipped with eight ultraminiature coax connectors (UMCCs) that interface with the AWG inputs *via* SubMiniature version A (SMA) and Bayonet Neill–Concelman (BNC) cables. This side also houses the two MUXs, along with the ADCs and DACs. The device side of the board (3.9b) includes the MCU and the input switches, which control whether the metasurface electrodes are driven by the ADC/DAC system or directly by the function generator. Metasurfaces can be easily connected to the board *via* an adapter PCB (Fig. 3.8a) that fits into the device socket, ensuring the board's reusability for multiple metasurfaces.

The bandwidth of the metasurface integrated into the PCB is measured directly through optical readout using a photodiode, when a square wave is applied to the metasurface. The -3 dB cutoff frequency is determined to be 5.4 MHz, consistent with the bandwidth measured electrically at the device socket pins of the PCB (Fig. 3.10). This result indicates that the bandwidth is entirely electronically limited, with the primary constraint being the MUXs used in the PCB design, as discussed earlier.

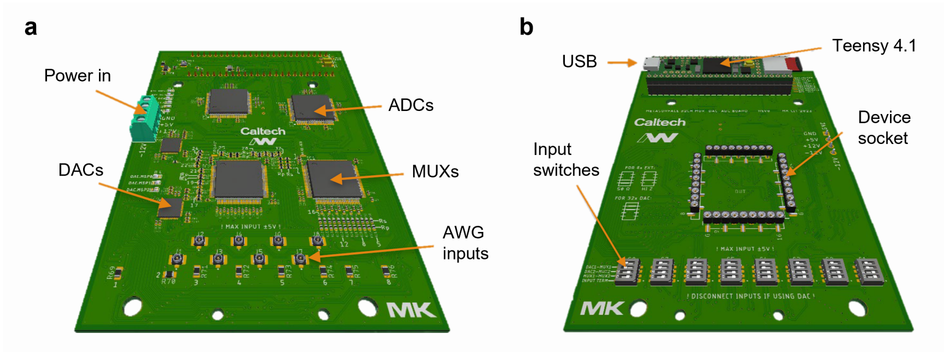

Figure 3.9: **High-frequency PCB for control of 32-electrode metasurface.** The PCB measures 3.6 × 4.6 inches. (a) IC side featuring the power source and eight ultraminiature coaxial connectors (UMCCs) that serve as inputs from the AWG. Key components include the analog-to-digital converter (ADC), digital-to-analog converter (DAC), and multiplexer (MUX). (b) Device side featuring the microcontroller unit (Teensy 4.1) with a USB interface. Input switches enable toggling between control *via* the AWG and the ADC/DAC system. The metasurface is connected to the board *via* a device socket using an adapter PCB.

Substituting the MUXs with higher-bandwidth components could enable the use of a similar PCB to probe the intrinsic frequency limit of the metasurface.

Quasi-static beam switching and steering

To demonstrate the added spatial versatility enabled by the increased number of electrodes and the PCB, we performed quasi-static beam switching and steering at various angles by modifying the spatial voltage profile applied to the metasurface. Figure 3.11a illustrates the two-level voltage profiles used to achieve beam switching at a wavelength of λ = 1490 nm. The repetition number (RN) is defined as the number of adjacent pixels with the same applied voltage. Experimental measurements (Fig. 3.11b) show tunable control over the diffraction angle, ranging from 17.9° (RN = 2) to 6.8° (RN = 5). When a uniform voltage is applied across the entire array (RN = 0), no diffraction is observed. By comparing the measured far-field intensity patterns to array factor calculations for metasurfaces with constant amplitude and varying amounts of phase modulation, we deduced that the metasurface exhibits a phase shift of approximately 80°. Considering the inherent coupling between phase and amplitude modulation in practical metasurface designs, the actual phase modulation might slightly exceed this value, compensating for some degree of amplitude modulation.

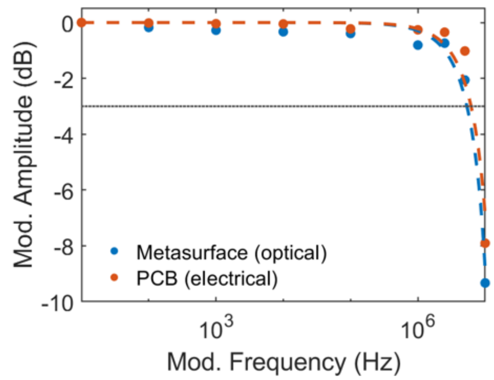

Figure 3.10: **Experimentally measured bandwidth of metasurface and high-frequency PCB.** Normalized modulation amplitude for metasurface integrated into PCB, driven by a square waveform. The metasurface modulation amplitude (blue) is measured through optical readout of the reflected signal using a photodiode, while the PCB modulation amplitude (orange) is measured electrically at the device socket pins. In both cases, the modulation amplitude is normalized to its value at 10 Hz. The gray dotted line indicates the −3 dB cutoff.

Despite the limited phase modulation, we demonstrated that asymmetric radiation patterns can be generated by applying distinct phase gradient profiles to the same metasurface (Fig. 3.11c). Calculated radiation patterns for these profiles (Fig. 3.11d) align well with the experimentally measured results (Fig. 3.11e).

These results confirm that, even with modest phase modulation, the metasurface and PCB setup can achieve tunable diffraction and steering, providing the desired spatial versatility. While quasi-static control cannot suppress the 0^{th} order diffraction with limited phase modulation, we will demonstrate in the next section that time-modulated control enables suppression of the 0^{th} spatial order of frequency-shifted light. This approach builds upon previous results with a two-electrode metasurface while incorporating enhanced tunability of the diffraction angle.

Tunable diffraction of frequency-shifted beams

To demonstrate tunable diffraction of frequency-shifted beams, we modulate the metasurface with a 12 Vp-p sinusoidal waveform at 1 MHz. We then drive the metasurface with two such waveforms, where one is phase-shifted by π, replicating the configuration previously shown in Fig. 3.7. By varying the repetition number, we achieve tunable diffraction of frequency-shifted beams, showcasing enhanced spatial versatility enabled by the increased number of electrodes. Unlike the earlier experiment performed with the two-electrode metasurface, this demonstration em-

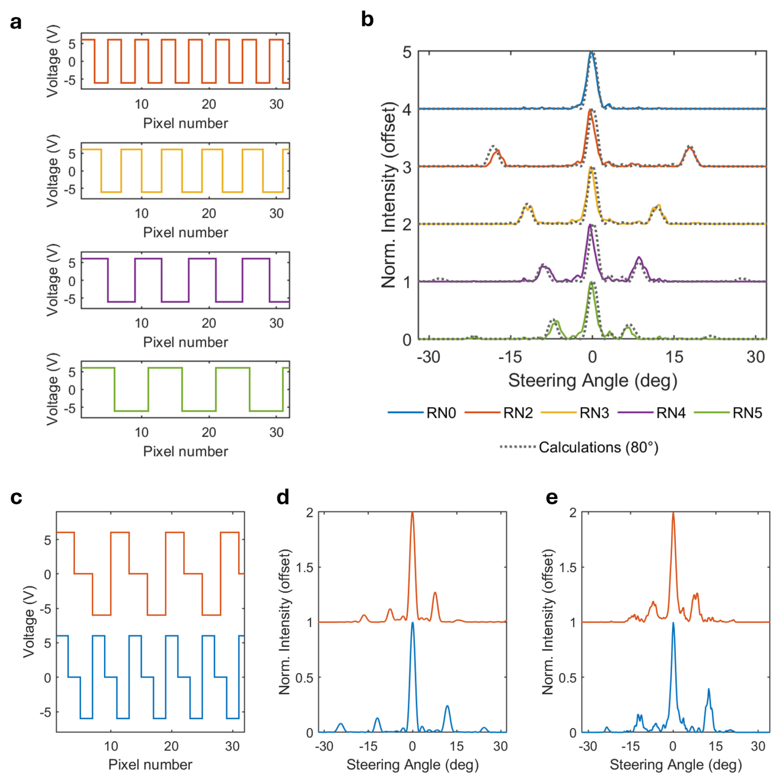

Figure 3.11: **Quasi-static beam switching and steering with 32-electrode metasurface.** (a) Two-level voltage profiles applied to the metasurface for tunable diffraction, with repetition numbers corresponding to RN = 2 (orange), 3 (yellow), 4 (violet), and 5 (green). Metasurface pixels are defined as unit cells addressable by individual electrodes (Fig. 3.8c). (b) Measured far-field intensity patterns associated with the voltage profiles shown in (a). For reference, we include the radiation pattern from the case where a uniform voltage is applied across all metasurface pixels (RN = 0). The dotted line represents the calculated far-field radiation pattern, assuming constant amplitude and a phase modulation of 80° between the two voltage levels. (c) Three-level voltage profile applied to metasurface, (d) calculated normalized far-field intensity pattern assuming phase values of 85°, 42.5°, and 0° for the three voltage levels, and (e) experimentally measured far-field radiation pattern. All intensity profiles are normalized to their maximal values and offset for visualization. Measurements and calculations were performed at a wavelength of λ = 1490 nm.

ploys a standard, non-optimized waveform to probe the metasurface response across multiple frequency harmonics. The increased number of frequency harmonics arise from the non-linear relationship between the applied voltage and amplitude and phase response of the metasurface.

Figure 3.12 presents the measured intensity as a function of frequency and angle for different RNs, corresponding to varying number of electrodes driven by the same time-varying waveform. Adjacent sets of electrodes are offset by half a waveform (π) to achieve diffraction of individual frequency harmonics. An overview of the four cases analyzed in Fig. 3.12 reveals that varying the RN alters the the diffraction angle across the harmonics. In contrast, applying a uniform time-modulated waveform across the entire metasurface results in no significant diffraction for any harmonic (Fig. 3.12d). Minor signals observed at the diffracted orders at 1 MHz are attributed to slight variations in the electrode response, as elaborated in Ref. [95]. These differences can accumulate over time, particularly during repeated measurements using two-level time-modulated voltage profiles with voltages near the device's breakdown threshold. This accumulation may lead to buildup of charge carriers in the ITO layer, causing changes in the optical response of specific electrodes [46].

To better illustrate the spatial response from the metasurface and differentiate between the spatio-temporal configurations, we examine the spatial intensity profile at frequency harmonics up to 4 MHz for the four configurations shown in Fig. 3.12. Beyond this range, the signal-to-noise ratio becomes too low to provide reliable information. The intensity profiles, displayed in linear scale in Fig. 3.13, reveal that when a uniform time-varying waveform drives the entire metasurface (Fig. 3.13a, RN = 0), all frequency-shifted light remains confined to the 0^{th} spatial order. However, for the metasurface driven by a a spatio-temporally varying waveform (Fig. 3.13b), selective diffraction is achieved at particular harmonic frequencies. Notably, the second harmonic at 2 MHz is selectively diffracted while the 0^{th} order at this frequency is suppressed. Our results show that by varying the repetition number, the diffraction angle of the frequency-shifted light can be varied from 9° to approximately 14°.

The observed diffraction at only the second harmonic indicates that the metasurface achieves a selective phase shift of approximately 180° at this frequency. As discussed previously in Section 3.2, a phase delay α between two driving waveforms imparts a phase $l\alpha$ to each harmonic l [95]. In our prior study with the two-electrode metasurface which primarily relied on amplitude modulation, this behavior could

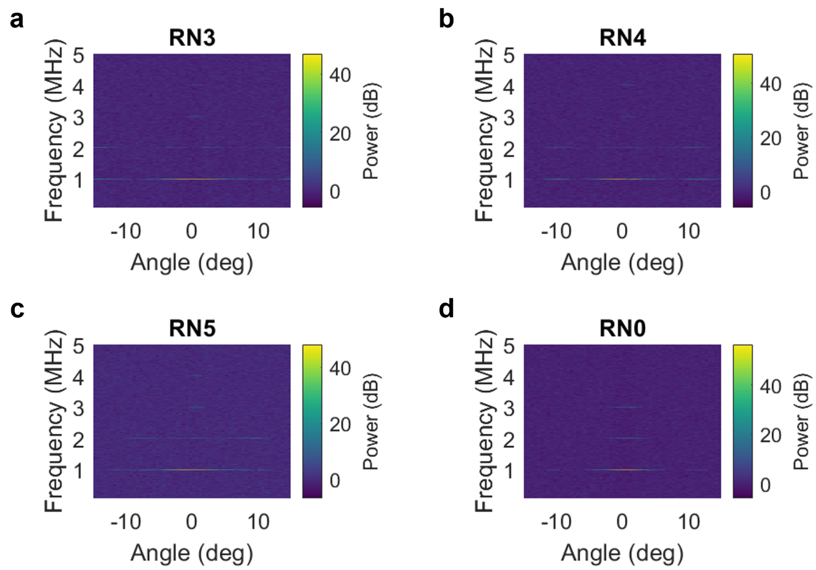

Figure 3.12: **Tunable space-time diffraction with varying repetition numbers.** Measured intensity of reflected light as a function of frequency and angle, plotted in log scale. A 12 Vp-p sinusoidal waveform is applied to the metasurface, with diffraction of frequency-shifted light achieved by offsetting the waveform applied to alternating sets of electrodes by half a period (π). Results are shown for (a) RN = 3, (b) RN = 4, (c) RN = 5, and (d) RN = 0, which represents the case where all antennas are modulated uniformly with the same waveform. The measurements are performed at a wavelength of λ = 1510 nm.

enable selective diffraction of odd harmonics based on the phase delay between adjacent electrodes [95]. For the 32-electrode metasurface studied here, the results suggest that the device exhibits covariation of amplitude and phase, leading to an effective phase delay of π at 2 MHz, enabling tunable diffraction for this harmonic.

3.6 Active multitasking: Multi-frequency multi-beam steering

One of the key benefits of spatio-temporal modulation in metasurfaces is the ability to encode information simultaneously in space and time, enabling multiplexing of channels using a single nanophotonic chip. In the previous experimental studies, we demonstrated how distinct frequency harmonics could be diffracted by configuring an active metasurface with phase-delayed driving waveforms. Specifically, in Ref. [95], we also showed that by phase-delaying individual fundamental frequencies of a Fourier series waveform across an interdigitated set of electrodes, we can achieve selective diffraction of desired harmonics. Building on this, we now explore general

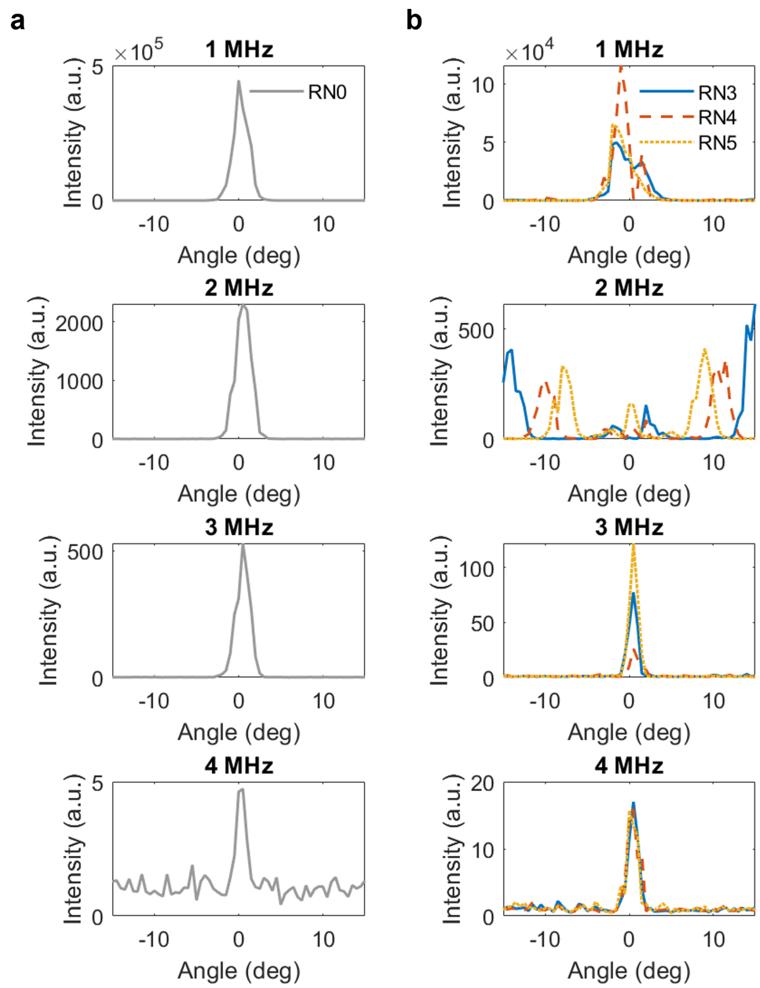

Figure 3.13: **Spatial intensity profiles at harmonic frequencies.** Intensity profiles at multiples of 1 MHz obtained from measurements shown in Fig. 3.12. (a) RN = 0 (gray) represents the case where the entire metasurface is uniformly modulated with a 1 MHz sinusoidal waveform. (b) RN = 3 (blue solid), 4 (orange dashed), and 5 (yellow dotted) correspond to the configurations where the metasurface is driven with two out-of-phase waveforms (π phase offset) applied across adjacent sets of electrodes, with RN defining the number of electrodes sharing the same waveform.

principles and strategies for adding frequency harmonics, multiplexing frequency channels, and steering different harmonics to different target angles.

When distinct waveforms with different fundamental frequencies are applied to metasurface elements in an interdigitated fashion, crosstalk between adjacent elements can produce undesired scattering at the generated frequency harmonics. One approach to mitigate this issue is to divide the metasurface into subarrays, each driven by distinct waveforms at a different frequencies. While this method eliminates crosstalk, it reduces the effective aperture of each frequency channel, leading to lower spatial resolution. An alternative strategy involves driving all metasurface elements simultaneously with multiple waveforms, each at a different frequency. In this configuration, spatial information can be independently controlled within each frequency channel by introducing phase delays at specific fundamental frequencies.

To illustrate metasurface control across multiple frequency channels, we consider two operational regimes: one where external voltage biasing results in pure phase modulation, and another where biasing produces pure intensity modulation. For pure phase modulation (Fig. 3.14a), driving all elements in-phase with multiple fundamental frequencies results in a frequency shift that corresponds to the sum of the fundamental frequencies. For instance, as shown in Fig. 3.14b, driving a metasurface with the sum of two sawtooth waveforms at 1 MHz and 2 MHz, respectively, each resulting in sawtooth phase modulation from 0° to 360°, produces a frequency-shifted reflected beam with its strongest harmonic at 3 MHz. This behavior arises because phase is encoded in the exponential term of an electromagnetic wave, as described in Eq. (3.3). Moreover, we note that with complete 360° phase modulation, the 0^{th} harmonic can be suppressed, as illustrated in Figs. 3.1 and 3.2.

In contrast, pure amplitude modulation (Fig. 3.14c) more closely resembles the experimentally demonstrated cases discussed earlier. Here, the 0^{th} harmonic cannot be suppressed, even when the minimal reflectance reaches 0%. Nevertheless, distinct frequency harmonics can be generated by applying sinusoidal waveforms. For example, driving the metasurface with a Fourier series waveform comprising fundamental frequencies at 1 MHz and 2 MHz results in multiplexed frequency harmonics at f_0, $f_0 + 1$ MHz, and $f_0 + 2$ MHz (Fig. 3.14d). The results shown here assume reflectance modulation ranging from 1% to 8%.

In this configuration, spatial information can independently be encoded into each harmonic without crosstalk between channels. For example, a metasurface modulated by a Fourier series waveform with fundamental harmonics at 1 MHz and 2 MHz can be programmed to leave the 1 MHz harmonic unchanged while incorporating a four-level spatial phase profile into the 2 MHz harmonic. This is achieved by introducing a phase offset of $\pi/2$ at 2 MHz between adjacent metasurface electrodes. Four distinct waveforms are required to modulate the metasurface in this case, resulting in the spatio-temporal reflectance profile shown in Fig. 3.14e. A

Fourier transform of this profile reveals the intensity distribution as function of frequency and polar angle (Fig. 3.14f), demonstrating selective steering of the second harmonic while maintaining specular reflection of the first harmonic. This method also enables encoding more complex spatio-temporal information across multiple harmonics, enabling a potential implementation of active multitasking metasurfaces for multi-frequency multi-beam steering or even simultaneous focusing and steering of beams using different frequency channels.

Implementing this concept experimentally faces two main challenges. First, the number of high-frequency waveforms that can be used to modulate the metasurface is inherently constrained by the capabilities of the driving electronics. In our current PCB setup, the metasurface can be driven with up to eight independent waveforms at MHz frequencies. Larger PCBs with increased number of channels could be implemented at the cost of a larger PCB form factor. Second, frequency multiplexing reduces intensity as energy is distributed across multiple channels. While space-time modulation increases the control and information densities, practical integration of frequency-multiplexed metasurfaces in applications will require high-efficiency to counteract intensity losses. Pathways to address this challenge are discussed in Section 3.7 as well as the subsequent chapters.

3.7 Outlook

Increasing the efficiency of frequency conversion

The conversion efficiency of the frequency harmonics reported in the experimental results discussed in this chapter was limited by two primary factors: (1) the reliance on amplitude modulation and (2) the inherent efficiency limitations in the plasmonic ITO-based metasurface used in this demonstration. We note that while, in principle, it would be possible to operate at a wavelength with higher phase modulation (λ = 1470 nm for the two-electrode metasurface discussed in Sections 3.3 and 3.4, see Appendix B.1), further experiments are necessary to confirm whether this level of phase modulation can be sustained at high frequencies. To date, phase measurements of metasurfaces have been reported only within the quasi-static operation regime. To evaluate the phase response at high frequencies, one approach would be to modulate the metasurface spatio-temporally and examine whether suppression of unmodulated specularly reflected light can be observed. By comparing the intensity of diffracted, frequency-shifted light to undiffracted, unmodulated light, it may be possible to approximate the effective phase modulation at that specific frequency. For greater accuracy, the associated reflectance modulation, which is measurable

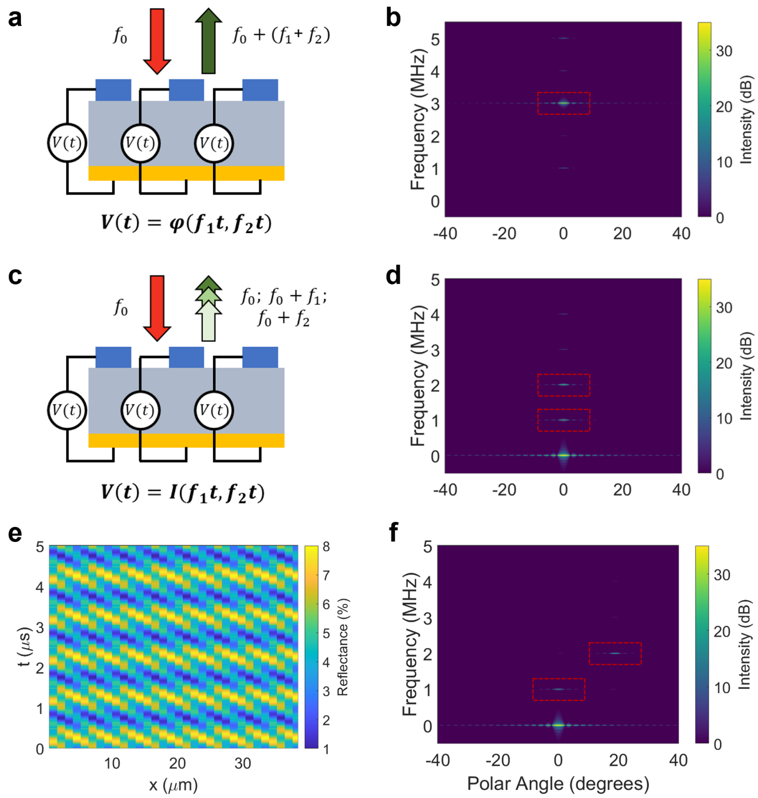

Figure 3.14: **Harmonic frequency control with phase and amplitude modulation.** (a) Schematic of metasurface driven with two time-varying waveforms, $f_1 t$ and $f_2 t$, producing pure phase modulation. The reflected beam is frequency-shifted by the sum of f_1 and f_2. (b) Calculated intensity as function of frequency and polar angle for a metasurface driven by the sum of two sawtooth waveforms with fundamental frequencies $f_1 = 1$ MHz and $f_2 = 2$ MHz, resulting in pure phase modulation ranging from 0° to 360°. (c) Schematic of metasurface driven by two time-varying waveforms, $f_1 t$ and $f_2 t$, producing pure intensity modulation. The reflected beam contains multiple frequency-shifted harmonics determined by the applied waveform. (d) Calculated intensity as function of frequency and polar angle for a metasurface driven by a Fourier series voltage waveform with fundamental frequencies $f_1 = 1$ MHz and $f_2 = 2$ MHz, resulting in intensity modulation from 1% to 8%. (e) Spatio-temporally varying reflectance profile for a metasurface driven by a Fourier series waveform with $f_1 = 1$ MHz and $f_2 = 2$ MHz. The second harmonic incorporates a four-level spatial phase profile, introducing a $\pi/2$ phase offset at 2 MHz between adjacent elements spaced 1.2 μm apart. (f) Calculated intensity as function of frequency and polar angle for the metasurface configuration described in (e). All calculations are performed at $\lambda = 1550$ nm. Red boxes in (b), (d), and (f) highlight frequency-shifted harmonics.

at high frequencies using an oscilloscope, should also be incorporated into this analysis. Alternatively, it may be possible to use phase imaging cameras, such as the Phasics wavefront-sensing cameras which may enable real-time phase imaging [130].

While achieving higher phase modulation could significantly enhance conversion efficiency, the reflectance of plasmonic ITO-based metasurface remains a critical limiting factor. To improve the total reflectance or transmittance of space-time modulation, novel active metasurface designs are required. The transparent conducting oxide (TCO)-based plasmonic platform employed in this work offers several advantages, including potentially large phase shifts, ease of electrical modulation with high spatial resolution, and rapid modulation speeds. However, absorption in the gold and ITO layers limits the platform's overall efficiency. Alternative materials, such as cadmium oxide (CdO) [74], have been proposed to address this issue and achieve higher efficiency in TCO-based platforms. Alternative modulation schemes employing low loss active materials include the use of electro-optic materials and liquid crystals. We note that liquid crystals are generally not suitable for space-time modulation, as they generally support low modulation frequencies ranging up to hundreds of Hz to few kHz [131]. Electro-optic materials can be modulated at higher frequencies, but they typically exhibit lower index modulation and therefore require advanced resonator designs to achieve significant reflectance or phase modulation. While design strategies incorporating various electro-optic materials are currently being investigated by many research groups, we will explore the use of barium titanate as an active material for transmissive in the subsequent chapter.

High-frequency limits of experimental metasurfaces

The 32-electrode metasurface integrated into the high-frequency PCB developed in this project exhibits a -3 dB bandwidth of 5.4 MHz. In the current setup, the modulation bandwidth is constrained by the multiplexers used in the PCB (AD8113). Replacing these components with higher-frequency multiplexers, such as the AD8114 or AD8115, could enable testing of metasurfaces with multiple waveforms at frequencies approaching $\sim$100 MHz or beyond. While the primary goal of this project was to demonstrate the proof-of-concept functionality of the PCB together with the metasurface, integrating these higher-performance components could be considered for future iterations now that the initial design has been validated.

Achieving higher modulation frequencies, however, is not solely dependent on the electronics. The design and material properties of the metasurface also play a crucial role. In principle, ITO-based metasurfaces could support larger modulation bandwidths through reduced metasurface footprints or through the implementation of two-dimensional antenna arrays that yield lower capacitance values [30]. Beyond ITO, alternative material platforms such as two-dimensional materials [132] or electro-optic materials [31] have been proposed to enable high-frequency modulation extending into the GHz regime. Together, advancements in both electronics and materials hold the potential to unlock higher-frequency capabilities for active metasurfaces.

Non-reciprocity using space-time modulation

The ability to independently control the spatial and spectral properties of light provides a promising pathway for designing nanophotonic elements that enable the violation of Lorentz reciprocity. Conventionally, nonreciprocity is achieved by applying a strong magnetic field, which necessitates bulky ferromagnetic materials and limits practicality for many applications. Spatiotemporal modulation, however, offers a more compact alternative by breaking time reversal symmetry without the need for large magnetic fields. To achieve significant spatial separation of light, which is a key requirement for optical isolation, the modulation frequency must approach the frequency of the incident light. As a result, most demonstrations of nonreciprocal space-time metasurfaces thus far have been in the RF domain [94, 121, 133, 134].

Recent advances in optical metasurfaces have achieved electrical modulation in the GHz regime [31] and could potentially be extended using the spatiotemporal modulation schemes outlined in this work to yield small spatial offsets. However, realizing larger spatial and spectral separations for applications like optical isolation would require novel optical designs. In this regard, optical pumping of space-time metasurfaces has emerged as an effective technique for achieving large spatial separation [115, 126].

3.8 Conclusions

In conclusion, we have demonstrated the experimental operation of near-infrared metasurfaces that are electrically modulated at MHz frequencies to generate desired harmonic spectra and independently diffract frequency harmonics in space. This result is made possible by recent advancements in the modulation frequency and degree of spatial phase gradient control achievable in active metasurfaces operating at optical frequencies. Initially, we employed a two-electrode ITO-based plasmonic metasurface operating at 1530 nm and modulated it with tailored MHz waveforms to create time-varying wavefronts that selectively excite desired frequencies while suppressing unwanted harmonics. The generated frequency harmonics were then spatially manipulated by introducing a phase delay corresponding to half the waveform period between the signals applied to each electrode.

Building on this, we extended the concept of spatiotemporal modulation to a metasurface with 32 individually addressable electrodes, enabling tunable diffraction of frequency harmonics. We designed a high-frequency PCB capable of taking up to eight inputs from a function generator and routing them to any of the 32 metasurface electrodes, allowing for the creation of more complex spatiotemporal wavefronts. This platform opens the door to advanced functionalities beyond tunable diffraction, such as steering and focusing of frequency-shifted light. Additionally, we outlined theoretical approaches to leveraging phase- or amplitude-modulated metasurfaces for implementing mathematical operations, such as addition of frequency harmonics, or for obtaining frequency multiplexed operation, and active multitasking.

The ability to generate and spatially manipulate frequencies within a single chip-scale device significantly enhances the control and information density of nanophotonic elements. While fundamental challenges remain, such as the need to improve modulation bandwidth and the efficiency of metasurface platforms, the methods and designs presented here offer a pathway for many applications in optical communication, sensing, and information processing.